

Mechanisms in the solution growth of free-standing two-dimensional inorganic nanomaterials

Cite this: DOI: 10.1039/c4nr00973h

Fei Wang and Xudong Wang*

Free-standing two-dimensional (2D) nanomaterials have attracted extensive and growing research interest owing to their exotic physical and mechanical properties, which have enabled their applications in electronics, optoelectronics, electrochemical and biomedical devices. Current synthesis strategies rely largely on top-down approaches such as etching and exfoliation. Among bottom-up approaches in literature, there lacks a systematic understanding of the mechanisms of 2D crystal growth, unlike one-dimensional nanomaterials whose growth mechanisms have been well documented. To date, the growth design of free-standing 2D nanomaterials has remained a case-by-case practice. This review focuses on the bottom-up solution synthesis of free-standing 2D nanomaterials and summarizes the general mechanisms and empirical methodologies that can lead to 2D crystal growth. A brief outlook on the development of synthesis and application of solution-grown 2D nanomaterials is also presented.

Received 21st February 2014
Accepted 9th April 2014

DOI: 10.1039/c4nr00973h

www.rsc.org/nanoscale

1. Introduction

Free-standing two-dimensional (2D) nanomaterials have drawn extensive and growing interest in the research frontier of nanoscience and nanotechnology.^{1,2} Their dimensionality can drastically alter their physical, chemical, and optical properties as compared to their bulk or other dimensional counterpart, which provides them with great potential in electronics, optoelectronics, electrochemical, and biomedical applications. The most representative examples are graphene and single-layer MoS₂, which have disparate electronic structures compared to their bulk counterpart, and have been demonstrated as candidates for advanced functional devices such as thin-film transistors, photodetectors, light-emitting diodes, and hydrogen reduction electrodes.^{3–5} In addition, 2D nanomaterials offer great mechanical flexibility (best exemplified by semiconductor nanomembranes^{6–8}) and are very fabrication friendly, which is essential to the realization of transparent and flexible electronics^{9–12} and conformal biomedical devices.^{13,14}

Despite their great scientific value and application potential, the success of 2D nanomaterials has been limited to only a few materials to date. The major challenge in exploring the properties and applications of the 2D nanostructure of a wider range of materials lies in the difficulty of their synthesis. Currently, a majority of 2D nanomaterials are prepared by either selective etching of sacrificial layers¹⁵ or exfoliation of crystals with an intrinsic layered structure.^{16,17} For materials without a layered crystal structure, strategies for the bottom-up growth of 2D nanostructures need to be developed to meet the demand for a

diverse portfolio of 2D nanomaterials. The growth of one-dimensional nanomaterials, namely, nanowires and nanotubes, can usually be well explained and rationally designed by established mechanisms such as catalyzed vapor–liquid–solid (VLS),¹⁸ vapor–solid–solid (VSS),¹⁹ and solution–liquid–solid (SLS) growth,^{20,21} growth kinetics anisotropy, and screw dislocation-driven growth.^{22,23} In contrast, there has yet to be a mechanism that explains a wide range of 2D crystal growth. To date, the growth design of 2D nanomaterials has remained a case-by-case practice, although a good number of syntheses of 2D nanomaterials have been reported.²⁴ An understanding of the driving force and fundamental principles that govern 2D crystal growth needs to be acquired to optimize the existing syntheses and extend them to untapped materials.

In this review, we focus on solution-based syntheses of 2D nanomaterials with their thickness ranging from a few hundred nanometers to a few atomic layers or a single atomic layer. Depending on the size, thickness, and flexibility, these 2D nanomaterials are referred to as nanomembranes, nanoplates, or nanosheets in literature. These terms are interchangeable, and we will use the names originally given by the authors of the cited literature. It would be a daunting task to include all the reports in this area. Our objective is to rather discuss the typical examples in detail and present the possible general growth mechanisms that could lead to 2D crystal growth by sorting these reports according to the growth mechanisms, which are either explicitly elucidated by their authors or reckoned by us. For those cases when the growth mechanisms are not clear due to limited experimental investigation, we link them by the similarities in their synthesis methods and crystal structures. In some examples, we also highlight the main differences between the syntheses of 2D nanomaterials and the growth of 1D

Department of Materials Science and Engineering, University of Wisconsin–Madison, Madison, WI 53706, USA. E-mail: xudong@enr.wisc.edu

morphology from the same or similar materials. We only look into bottom-up approaches in order to discuss what could drive 2D crystal growth; therefore, well-documented exfoliation methods for layered-structure crystals such as graphene, boron nitride, and transition-metal dichalcogenides are not covered. We will also feature a surfactant monolayer-guided approach developed by our group for producing large-area, free-standing nanomembranes. Although we sort all the syntheses in four categories (Section 2 to 5), most of them do not exclusively belong to a single category. These four categories are rather four different aspects of one framework. In the end, a brief review of the applications of 2D nanomaterials and an outlook on the development of novel synthesis strategies of 2D nanomaterials are given.

2. 2D oriented attachment

Oriented attachment is a non-classical crystal growth mechanism and often produces nanocrystals with well-defined shapes and stringent size control. There have been a number of good

reviews on this mechanism.^{25–27} In oriented attachment, nanoparticles, often only a few nanometers in size, can rotate themselves continuously until they find an aligned crystallographic orientation, and then irreversibly attach to one another by lateral atom-by-atom addition at the interface. The oriented attachment mechanism itself does not predict the dimensionality of crystal growth. However, since the interactions between these primary nanoparticles are strong and highly direction-specific,²⁸ controlling the availability of particular crystallographic facets for oriented attachment could lead to directional and anisotropic crystal growth. For example, restricting oriented attachment to two crystallographically equivalent but oppositely oriented facets could lead to a head-to-tail attachment that grows linear^{29,30} or zigzag-type 1D nanomaterials.³¹ Similarly, allowing oriented attachment only on facets whose normal directions are in the same plane would lead to the growth of 2D nanomaterials without increasing the thickness.

Schliehe *et al.* reported (100) facet-exposed PbS nanosheets by oriented attachment. The standard synthesis procedure for PbS, in which lead acetate, thioacetamide, oleic acid, and tri-*n*-

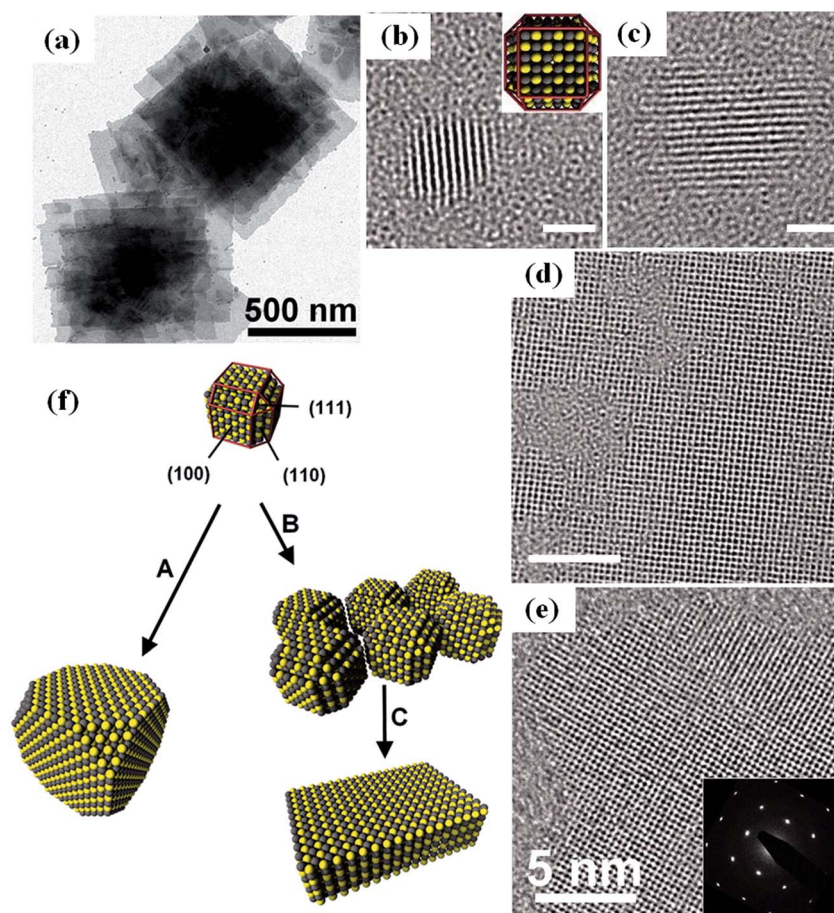


Fig. 1 (a) TEM images of PbS nanosheets in stacks. (b)–(e) High-resolution TEM images showing the process of the growth of nanosheets by oriented attachment. (b) A single primary nanoparticle with the inset showing all major facets: (100), (110), and (111). Scale bar = 2 nm. (c) Three nanoparticles attached as one with a perfect lattice match. Scale bar = 2 nm. (d) Large-scale attachment with pores in the nanosheet. Scale bar = 5 nm. (e) Nanosheet without pores; the inset is the corresponding electron diffraction pattern, showing the exposed (100) facets. (f) Illustration of the proposed process of the oriented attachment of PbS nanosheets. Reproduced with permission from American Academy of Arts and Sciences from ref. 32, Copyright 2010.

octylphosphine are added to diphenylether, typically produces nearly spherical PbS nanoparticles.³² The major difference in the synthesis of PbS nanosheets by Schliehe *et al.* was the use of chlorine-containing compounds such as 1,2-dichloroethane (DCE) as a co-solvent. Fig. 1a shows a TEM image of stacked PbS nanosheets about 500 nm in size. The oriented attachment mechanism during the growth of PbS nanosheets was demonstrated by monitoring the evolution of crystals by an HRTEM study. As shown in Fig. 1b, the crystal growth started with the appearance of ~ 2.8 nm PbS nanoparticles. Fig. 1c shows an aggregate of three nanocrystals bonded together in a way that their crystallographic orientations were perfectly matched. The nanoparticles could assemble on a much larger scale with pores within the sheets (Fig. 1d), and these pores were then filled by recrystallization. The corresponding electron diffraction pattern showed that the exposed facet was (100) (Fig. 1e). Absorption and emission spectra also supported the appearance and disappearance of PbS nanoparticles from 50 to 70 seconds into the reaction. The authors elaborated the process of the oriented attachment of PbS nanoparticles and pointed out that the oriented attachment occurred exclusively between the (110) facets. The process is illustrated in Fig. 1f. The initial PbS nanoparticles have a truncated cuboctahedron shape (the top particle in Fig. 1f) with 6 (100), 8 (111), and 12 (110) facets. Due to the fast growth of the (110) facets, the nanoparticles would normally grow bigger into a truncated octahedron without the (110) facets being exposed (growth route A). The addition of chlorine compounds altered the kinetics of nucleation and growth, yielding ~ 3 nm nanoparticles with exposed (110) facets available for oriented attachment (growth route B). Oriented attachment through the (110) facets gave an egg-tray structure of particles, and flat nanosheets formed thereafter *via* surface reconstructions (growth route C). The other requirement of this 2D growth is to thwart the particle attachment along the normal direction of the nanosheet's surface. This was attributed to the dense and ordered bonding of oleic acid on the surface of nanosheets.

Oriented attachment can also occur subsequent to a mis-oriented attachment driven by the relaxation of stress at the incoherently attached interfaces.³³ Yu *et al.* synthesized single crystal CeO₂ nanosheets in 95 °C aqueous solution by oriented attachment.³⁴ Fig. 2a shows a TEM image of the nanosheets, which are a few hundred nanometers in size and 2 nm in thickness. CeO₂ nanoparticles (2 to 2.5 nm) were found 15 minutes into the reaction, and after 75 minutes, a-few-hundred-nanometer-wide, a-few-nanometer-thick nanosheets were obtained. It was found that polycrystalline nanosheets were also present after 15 minutes of reaction. These mis-aligned nanoparticles transformed into single crystal nanosheets as the reaction proceeded. The key to successful nanosheet growth was the use of a syringe pump to add Ce(NO₃)₃ evenly and slowly into the reactor over 75 minutes of reaction time. Control experiments, in which Ce(NO₃)₃ was added all at once, resulted in only nanoparticles over 5 nm in size. The authors concluded that the formation of small-sized (2 to 2.5 nm) CeO₂ nanoparticles was a prerequisite for the oriented attachment. This agrees with Shen *et al.*'s observation that the primary Cu₂S nanoparticles larger than 5 nm could not grow into

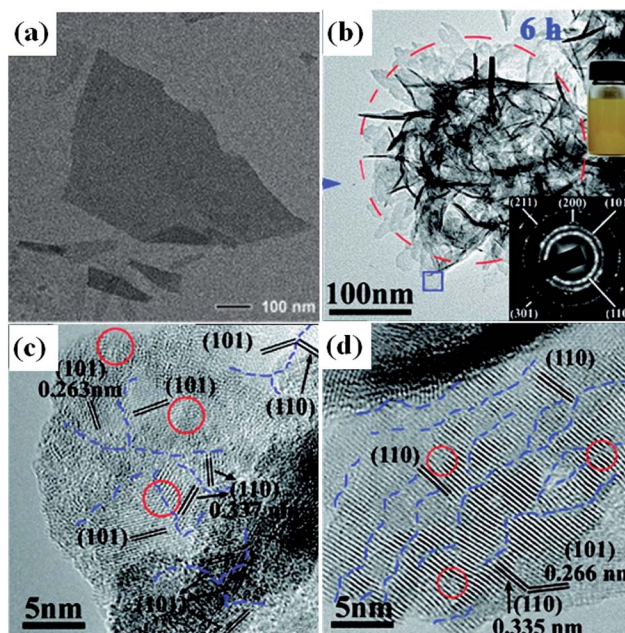


Fig. 2 TEM images of (a) CeO₂ nanosheets. (b) Aggregates of SnO₂ nanosheets. The upper inset is a photo of the SnO₂ nanosheet suspension, and the lower inset is the electron diffraction pattern. (c) SnO₂ nanosheets obtained after a reaction time of 4 hours with polycrystalline nature. (d) SnO₂ nanosheets obtained at 6 hours with a single-crystalline nature. (a) Reproduced from ref. 34 with permission from Wiley, Copyright 2010. (b)–(d) Reproduced with permission from American Chemical Society from ref. 36, Copyright 2012.

nanorods or nanodiscs *via* oriented attachment, unlike smaller nanoparticles.³⁵ However, the reason for the slow injection of precursor producing small-sized CeO₂ nanoparticles was not discussed. It would also be interesting to see how the flow rate of the precursor in the syringe pump would affect the size of the primary nanoparticle and the process of their oriented attachment.

Wang *et al.* synthesized rutile SnO₂ nanosheets in a solvothermal method and identified oriented attachment as the formation mechanism. This is another example that mis-aligned nanoparticles can rotate themselves and become single crystals. In their synthesis, SnCl₂·2H₂O was used as a Sn precursor and ammonia or urea was also added into an ethanol–water mixed solvent.³⁶ The solvothermal process was conducted at 120 °C for 48 hours. The SnO₂ nanosheets were 100 nm in lateral dimension and ~ 5 nm in thickness, as shown in Fig. 2b. The formation of SnO₂ started with the formation of poorly crystallized Sn₆O₄(OH)₄ prior to the hydrothermal treatment. TEM characterization of reaction products at different reaction times revealed that the decomposition of Sn₆O₄(OH)₄ during the hydrothermal process yielded clusters of randomly oriented SnO₂ nanoparticles, which rotated and fused into SnO₂ nanosheets. Fig. 2c shows a TEM image of the 4 hour products with multiple grains present in the nanosheet. After 6 hours, the reaction completely converted the nanosheets into a single crystal (Fig. 2d). Prior to this work, Li *et al.* used a similar method and obtained slightly larger (100–200 nm) rutile SnO₂ nanosheets and similar thickness (2–3 nm) with much better

crystallinity.³⁷ The difference in their synthesis was the use of NaOH in place of ammonia or urea and a higher temperature (180 °C). The formation mechanism was not discussed, but they did point out that the exposed (110) facet had a lower surface energy than any other major facets. Given the significant similarity between the two syntheses, the propensity for oriented attachment in SnO₂ systems³⁸ and the ubiquity of oriented attachment in hydrothermal synthesis, it is reasonable to believe that the SnO₂ nanosheets synthesized by Li *et al.* were formed by oriented attachment. We hypothesize that the oriented attachment between the non-(110) facets in rutile SnO₂ outrivalled the oriented attachment between the (110) facets; therefore, (110) facet-exposed nanosheets were obtained.

3. 2D growth driven by screw dislocations

Screw dislocation-driven growth is a fundamental crystal growth mechanism that exists in a vast variety of materials and in different supersaturation regimes. It is particularly prominent at low supersaturation when layer-by-layer growth and dendrite growth are suppressed. In screw dislocation-driven

growth, the axial screw dislocations provide self-perpetuating steps, which propagate in a spiral trajectory around the Burgers vector of the screw dislocation. It has been demonstrated as one of the predominant mechanisms that explain the 1D crystal growth of many materials.^{22,23,39,40} However, crystal growth involving screw dislocations does not necessarily lead to 1D materials; moreover, crystal growth rarely occurs by a single mechanism. Thus, the competition between spiral growth and lateral growth essentially dictates the final morphology of crystals.

Morin *et al.* reported the growth of zinc hydroxyl sulfate (3Zn(OH)₂·ZnSO₄·0.5H₂O, ZHS) nanoplates driven by screw dislocations.⁴¹ In a typical synthesis, aqueous solutions of 3 mM ZnSO₄, 3 mM Zn(NO₃)₂ and 6 mM methylenetriamine (HMT) were heated at 95 °C for 2 hours and a silicon substrate was used to collect the products. SEM images (Fig. 3a) show that the products were hexagonal nanoplates with diameters of 10–20 μm and thicknesses of 50–100 nm. Characterization using SEM imaging (Fig. 3b) and AFM topography scan (Fig. 3c) show that all nanoplates have the helical surface topology, which is a characteristic of screw dislocations. Bright-field TEM images (exemplified by Fig. 3d) of many of these nanoplates exhibited

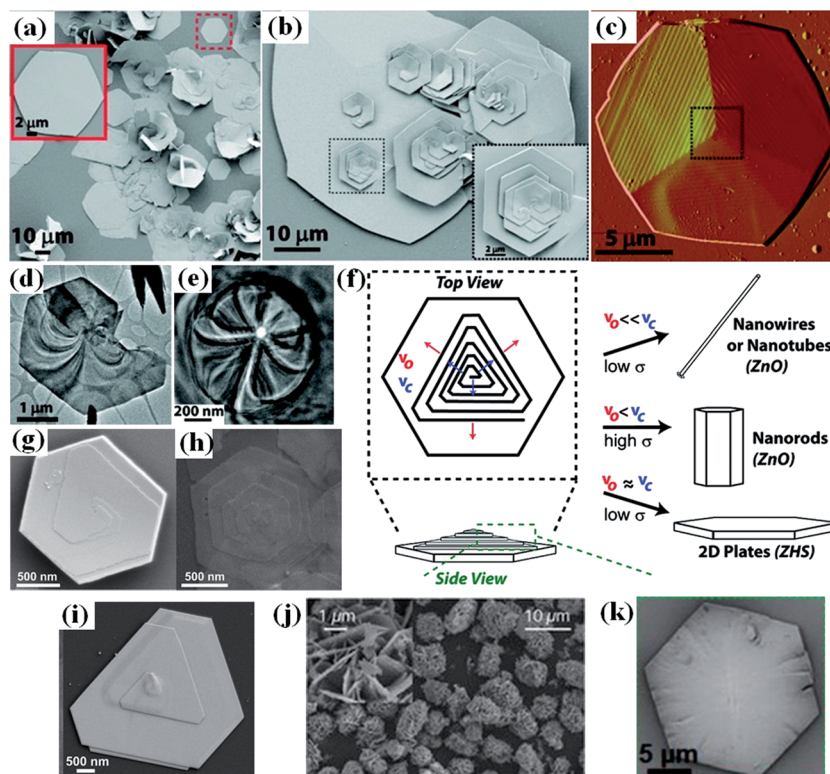


Fig. 3 (a) SEM image of hexagonal ZHS nanoplates. The inset is a higher magnification image of one with a flat surface. (b) SEM image of ZHS nanoplates with surface hillocks. The inset is a higher magnification image of one of the hillocks. (c) AFM topography scan showing the steps of the hillock. (d) TEM image of a ZHS nanoplate with contrast contours usually explained as bend contours. (e) TEM image of a ZHS nanoplate with contrast contours and an open core that is associated with screw dislocations. (f) Schematic illustration of the two growth velocities, ν_o and ν_c , during screw dislocation-driven growth. The degree of supersaturation and the relative strength between ν_o and ν_c lead to different morphologies. (g)–(i) SEM images of α -Co(OH)₂, Ni(OH)₂, and Au nanoplates synthesized from screw dislocation-driven growth. (j)–(k) CuGaO₂ nanoplates synthesized by Srinivasan *et al.* (j) and by Forticaux *et al.* (k) by using a modified synthesis condition guided by the framework presented in (f). (a)–(i) and (k), Reproduced with permission from American Chemical Society from ref. 41 and 43, Copyrights 2011 and 2013, respectively. (j) Reproduced with permission from Royal Society of Chemistry from ref. 42, Copyright 2008.

contrast contours (commonly explained as bending contours), which are associated with thin nanoplates conforming to the uneven TEM grid. Here, the authors reasoned that some of the contrast contours were actually resulted from strains associated with screw dislocations that perturbed the crystal lattice, as suggested by the existence of open cores at the center of the contours (Fig. 3e).

To elucidate the screw dislocation-driven 2D spiral growth motion and formation process of surface hillocks, the lateral growth velocity at the steps on the dislocation hillocks was discussed. In Fig. 3f, the lateral growth velocity of steps at the core was labeled as ν_c , and that at the outer edges of the dislocation hillocks was labeled as ν_o . If ν_o is much less than ν_c (possibly due to more adsorbed surfactants or slower mass transport), newly generated steps would quickly catch the earlier formed base, producing 1D materials with step-free side facets. If ν_o is equal to ν_c , all steps would propagate at the same velocity; thus, the steps would spread in 2D. It was also pointed out that low supersaturation was needed to suppress layer-by-layer growth and achieve the screw dislocation-driven 2D growth. The authors also synthesized α -Co(OH)₂, Ni(OH)₂ and Au nanoplates using modified procedures from literature. α -Co(OH)₂ and Ni(OH)₂ were produced in high density on substrates and similar surface hillocks were observed as shown in Fig. 3g and h, indicating screw dislocation-driven growth in both cases. Au nanoplates were also obtained with a high density, but their shape and size exhibited a large variation and only a small portion clearly showed dislocation spirals (Fig. 3i). While this could be a result of mixed growth mechanisms, it was argued that the dislocation step edges might be too small to resolve empirically on the Au nanoplates without conspicuous hillocks.

CuGaO₂ nanoplates were also grown by screw dislocations. In an earlier synthesis by the hydrothermal method, Srinivasan *et al.* produced aggregates of few-hundred-nanometer-sized CuGaO₂ nanoplates as shown in Fig. 3j.⁴² Guided by the rationale that low supersaturation favors screw dislocation-driven 2D growth, Forticaux *et al.* modified Srinivasan's synthesis procedure by reducing the precursor concentration (and thus the supersaturation) and replacing ethylene glycol with ethylenediamine, and obtained CuGaO₂ nanoplates with a much larger lateral dimension as shown in Fig. 3k.⁴³

There are also examples where 2D screw dislocation-driven growth could be responsible for the formation of 2D nano-materials but were not explicitly discussed. Viswanath *et al.* conducted a systematic study on the hydrothermal synthesis of various metal nanoplates, including Au, Ag, Pt, and Pd.⁴⁴ The change in the Gibbs free energy (ΔG) of each reaction at different pH values and temperatures was calculated for each reaction of the corresponding metal nanoplates. In these syntheses, no surfactant molecules were used and the control over morphology was achieved solely by tuning ΔG through the control of precursor concentration, pH value, and reaction temperature. The authors proposed two growth modes in these syntheses: continuous growth mode for 3D materials at a high driving force and 2D nucleation mode for nanoplate growth at a low driving force. It was argued that the 2D nucleation mode

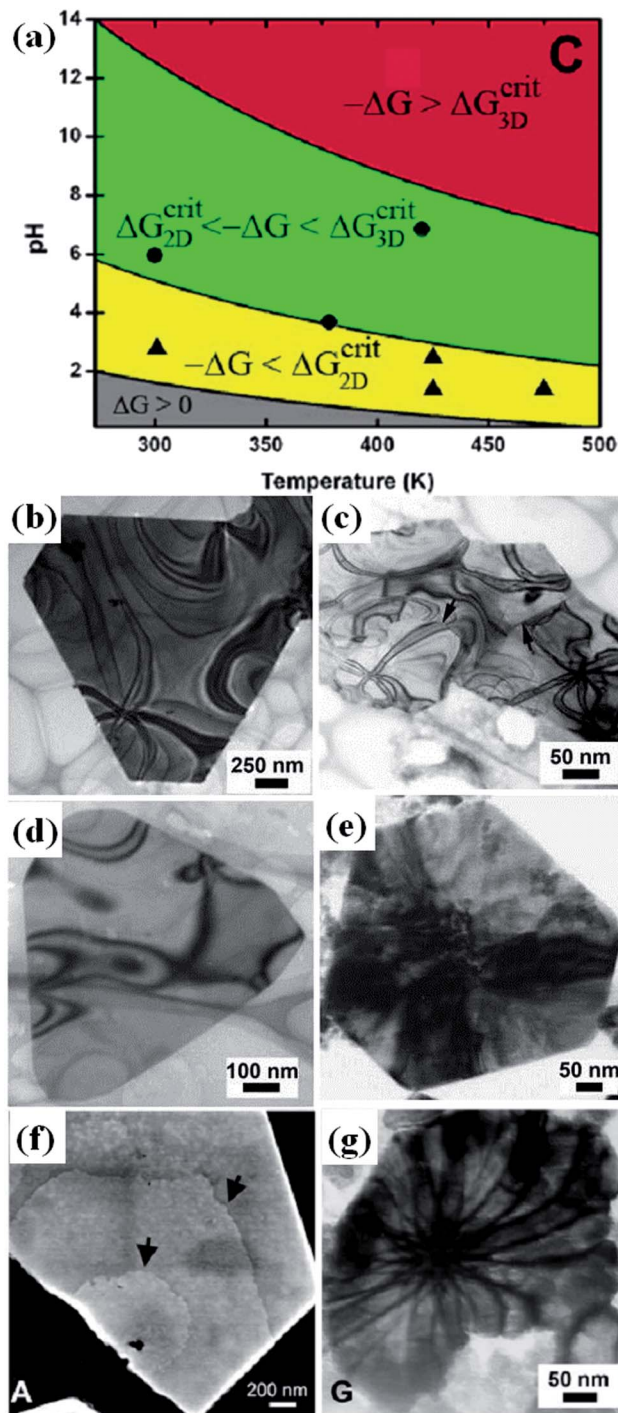


Fig. 4 (a) pH-temperature diagram showing regions of different supersaturations in the hydrothermal synthesis of Au nanostructures with 1 mM Au precursor. The curves separating different colored regions are iso-supersaturation lines. Dots and triangles represent experiments in which 3D and 2D products were produced, respectively. (b)–(e) TEM images of Au, Pt, Ag, and Pd nanoplates, respectively, with visible bend contours. (f) SEM image of Pt nanoplates, which have surface hillocks. (g) TEM image of Pt nanoplate with spider-like contours indicating screw dislocation-driven growth. Reproduced with permission from IOP Publishing from ref. 44, Copyright 2008.

has to rely on the formation of steps and a lateral motion of steps on the surface. Fig. 4a is a pH-temperature diagram that illustrates driving force regimes, in which the 2D nucleation mode (yellow) and the 3D continuous growth (red) is operative for the growth of Au using 1 mM HAuCl₄ solution, and the green region represents the transition regime. A series of experiments were carried out at different pH values and temperatures, which yielded nanoplates and irregularly shaped particles labeled by triangular and spherical dots, respectively, on the diagram. The critical value for 2D nucleation is defined as $\Delta G_{2D}^{crit} = \sigma g/a$, where σ is the interfacial energy between the crystal and the medium, g is a measure of the diffuseness of the interface (taken to be 1 for a sharp interface), and a is the monatomic step height on the surface. At a lower temperature and a low pH value (yellow region) where the change in the Gibbs free energy is smaller than ΔG_{2D}^{crit} , metal nanoplates were obtained. The experiment results were in accordance with calculations of the Gibbs free energy. A similar diagram for the synthesis of Ag nanoplates was also presented in their report, and consistent results were obtained. Fig. 4b–e are the SEM images of Au, Pt, Ag, and Pd nanoplates, respectively. Bend contours were observed in all the cases.

A closer look at the surface of these nanoplates by secondary-electron image (Fig. 4f for Pt) revealed the surface steps. Bright-field TEM image (Fig. 4g) showed that some of the nanoplates have spider-like contrast contours. Both are characteristics of screw dislocation-driven growth. Although Viswanath *et al.* described the surface steps as 2D nucleation, it is very likely that at least some of these nanoplates were grown by screw dislocations. Their mechanism uses ΔG to describe the crystal growth in 2D and 3D, which is equivalent to the supersaturation analysis provided by Morin *et al.*, as shown in Fig. 3f. Both arguments agree with each other on the dominant role of low supersaturation in driving 2D crystal growth. Unlike preferential adsorption, Morin *et al.* pointed out that the role of surfactants and inorganic ions in screw dislocation-driven 2D growth is to modify the lateral growth velocity of screw dislocation steps.

4. Surfactant-assisted synthesis of 2D nanomaterials

Surfactants are pervasively used in tuning the morphology of inorganic nanomaterials, from 1D to 3D. In this section, we introduce three different roles that surfactants may play in the synthesis of 2D nanomaterials.

4.1. Preferential adsorption

Although sometimes over-emphasized, preferential adsorption is perhaps the most commonly cited concept that has been used to explain the role of surfactants in the synthesis of inorganic materials, including 1D nanomaterials and nanocrystals with defined facets.^{45–47} The adsorbed species can be surfactant molecules (including polymer surfactants), inorganic ions, or small molecules. They slow down the crystal growth of certain crystal facets, on which surfactant molecules are adsorbed, while promoting the growth of other facets.

Huang *et al.* reported a synthesis of palladium nanosheets *via* a solvothermal method using palladium(II) acetylacetonate, PVP, and a halide salt dissolved in a solvent such as dimethylformamide or benzyl alcohol.⁴⁸ The reaction was conducted in a glass pressure vessel that was filled with CO to 1 bar and maintained at 100 °C for 3 hours. This process yielded well-defined hexagonal nanosheets with controllable edge lengths from 20 to 160 nm (Fig. 5a), leading to tunable surface plasmon resonance (SPR). The inset picture of Fig. 5a shows a dispersion of Pd nanosheets in ethanol with a SPR-induced blue color. Similar to Rh nanosheets, the exposed surface of Pd nanosheets was the (111) facet. Without CO, only twinned nanoparticles were obtained. It was believed that the strong adsorption of CO molecules on the (111) planes of Pd crystals suppressed the growth along the [111] direction. The presence of CO adsorption on the (111) surfaces of freshly prepared Pd nanosheets was confirmed by CO stripping voltammetry. Fourier transformation infrared (FTIR) studies indicated that CO was adsorbed in a bridge configuration. PVP was used to stabilize the nanosheets from aggregation. When PVP was absent, aggregates of irregularly shaped Pd nanosheets were received. The halide salt used in the synthesis could be a variety of compounds, including cetyltrimethylammonium bromide (CTAB) and NaX (X = Cl, Br, I). The role that halide ions played was to define the hexagonal shape of the nanosheets by binding to the (100) planes (side surfaces of hexagons).

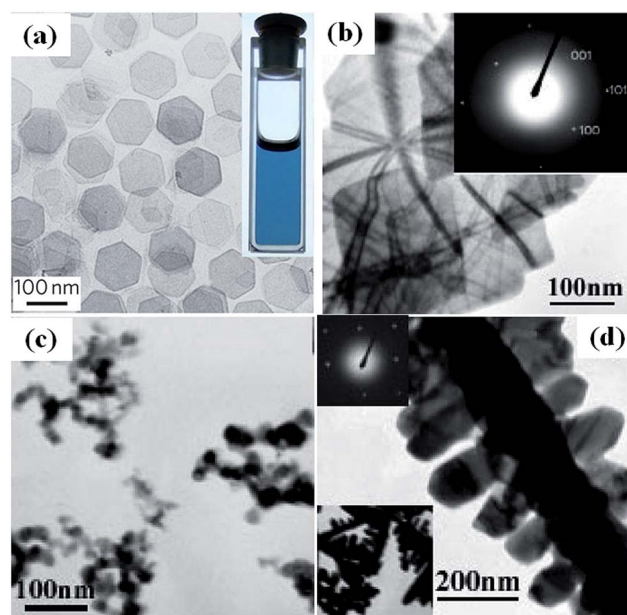


Fig. 5 TEM images of (a) Pd nanosheets with a well-defined hexagonal shape. The inset is a picture of a cuvette Pd nanosheet dispersed in ethanol, which forms a blue ink. (b) BiVO₄ nanosheets with a monoclinic crystal structure and (010) facets exposed. (c) BiVO₄ nanoparticles with a tetragonal crystal structure at the initial stages of the synthesis. (d) Fish bone-like aggregates of the tetragonal crystal structure. The upper inset is an electron diffraction pattern, and the lower inset is a lower-magnification image. (a) Reproduced with permission from Nature Publishing Group from ref. 48, Copyright 2011. (b)–(d) Reproduced with permission from American Chemical Society from ref. 49, Copyright 2006.

Zhang *et al.* prepared monoclinic BiVO_4 nanosheets with a size of a few hundred nanometers and a thickness of 10–40 nm.⁴⁹ Fig. 5b shows a TEM image of the BiVO_4 nanosheets. The inset is the corresponding electron diffraction pattern, revealing that the (010) planes are the exposed facets. In their hydrothermal synthesis, a metathesis reaction between $\text{Bi}(\text{NO}_3)_3 \cdot 5\text{H}_2\text{O}$ and NH_4VO_3 was employed. In addition, sodium dodecylbenzene sulfonate (SDBS) was used to control the morphology. The hydrothermal synthesis was performed at 200 °C for 1.5 hours. The authors believed that BiVO_4 nanosheets were grown by oriented attachment, which was supported by investigating samples collected at different reaction time intervals. A rather intriguing observation of the synthesis was that the initial BiVO_4 nanoparticles were in a tetragonal phase, whereas the final BiVO_4 nanosheets were monoclinic. Fig. 5c shows a TEM image of the initial tetragonal BiVO_4 nanoparticles. In literature, a typical practice in the hydrothermal synthesis of BiVO_4 (not in 2D) usually involves an alkaline (such as ammonia or NaOH) to adjust the pH value to the basic range where the monoclinic phase is obtained. In this synthesis, the absence of an alkaline might be the reason for the appearance of the tetragonal phase in the initial stage, as it was reported that a lower pH value favors the tetragonal phase.⁵⁰ It was not clear how the phase transformation occurred and how the phase transformation is related to the process of oriented attachment between tetragonal nanoparticles. Nevertheless, it was clear that the presence of SDBS had certainly influenced the kinetics of the BiVO_4 growth and the phase transformation. In control experiments when SDBS was not added, fish bone-like particle aggregates were obtained. No phase transformation from tetragonal to monoclinic was observed (Fig. 5d), and the tetragonal structure is shown in the inset of Fig. 5d. Li *et al.* reported that the formation of micelles of CTAB can alter the morphology of hydrothermal BiVO_4 from nanorods to nanoplates.⁵¹ However, in the case discussed here, the amount of SDBS added was much lower than its critical micelle concentration (CMC); thus, the micro-emulsion effect could be ruled out. The authors proposed that the atom density on the (010) plane is larger than that on the other planes. The preferred adsorption of dodecylbenzene sulfonate ions on the (010) plane affected the way that tetragonal BiVO_4 nanoparticles aggregated.

4.2. 2D alignment of surfactants

While the idea of preferential adsorption places its focus on the interaction between surfactant molecules and crystal facets, the inter-molecular interaction between surfactant molecules may provide another platform for surfactant-assisted 2D crystal growth.

Rhodium has a face-centered cubic (fcc) structure. Jang *et al.* prepared (111) plane-oriented ultrathin Rh nanosheets (thickness: 1.3 nm).⁵² In a typical synthesis, rhodium carbonyl chloride dimer, $[\text{Rh}(\text{CO})_2\text{Cl}]_2$ was dissolved in oleylamine, and the solution was heated at 50 °C for 10 days without stirring. As shown in Fig. 6a, the shape of the Rh nanoplates varied from triangle to quadrangle and all had 60° or 120° corners. These nanoplates could exhibit a self-assembled packed structure in

the range of tens of microns (Fig. 6b). Thickness measurements gave a statistical value of 1.3 ± 0.2 nm. It was noted that the formation of 1D molecular chains of Rh precursors played an important role in the formation of Rh nanoplates. Adding $[\text{Rh}(\text{CO})_2\text{Cl}]_2$ to oleylamine led to the formation of $\text{Rh}(\text{CO})_2\text{Cl}(\text{oleylamine})$ complexes. The metal–metal interaction between $\text{Rh}(\text{CO})_2\text{Cl}(\text{oleylamine})$ complexes was confirmed by the appearance of a new broad shoulder band at 500 nm in the UV-Vis absorption spectra of the precursor solution. A high concentration of precursor solution (from 1 mM to 10 mM) resulted in increased intensity of the shoulder band (Fig. 6c). Fig. 6d illustrates the formation process of the Rh nanoplates. In the molecular chains of $\text{Rh}(\text{CO})_2\text{Cl}(\text{oleylamine})$, the coordinated oleylamines would be located both up and down. The chains interact with each other *via* the van der Waals forces between the alkyl groups in oleylamines; thus, the molecular chains would assemble side by side to form a 2D precursor complex. IR studies showed that CO ligands in the complex were gradually delegated in the oleylamine solution. The excess amines gradually reduced the $\text{Rh}(\text{i})$ forming cationic radicals, during which Cl was subtracted from the precursors. Rh nanoplates were finally formed after the reduction. To support this mechanism, the length of the alkyl chains was reduced to dodecyl, octyl, and butyl, and the relative number of observed 2D plates to 1D rods was significantly reduced. Fig. 6e is a TEM image of the products using dodecylamine as the solvent. The formation of 1D products and smaller nanosheets shows that weaker van der Waals interactions yielded less 2D crystal growth. It is noteworthy that the 2D network of precursors guided by oleylamines was quite delicate. Increasing the reaction temperature from 50 to 70 °C significantly increased the amount of isotropic nanomaterials. This result confirmed that the weak interaction between the surfactant molecules was the driving force for 2D crystal growth.

4.3. Surfactant monolayer-guided synthesis

Template growth is widely practiced in controlling the morphology of nanomaterials. This is particularly true in growing 1D nanomaterials, *i.e.*, nanowires and nanotubes. Directing the precipitation of precursors in confined spaces, such as pores in anodized aluminum oxide (AAO), results in confined morphology replicative of the templates.^{53–55} In fact, this is often the first successful way of producing the 1D form of a material before a spontaneous 1D growth method is discovered. Direct application of templates in the growth of 2D nanomaterials seems difficult due to the unavailability of 2D templates with accessible nanoscale planar spacings. On the other hand, the mere use of a single planar surface, such as a substrate, as a 2D template does not necessitate conformal crystal growth in 2D. Therefore, guiding 2D crystal growth by templates requires a more subtle design of templates, which often involves chemical interactions between the template and target materials.^{56,57}

As discussed in Section 4.1, surfactant molecules could be selectively adsorbed on particular crystallographic facets and guide 2D crystal growth. Another important behavior of

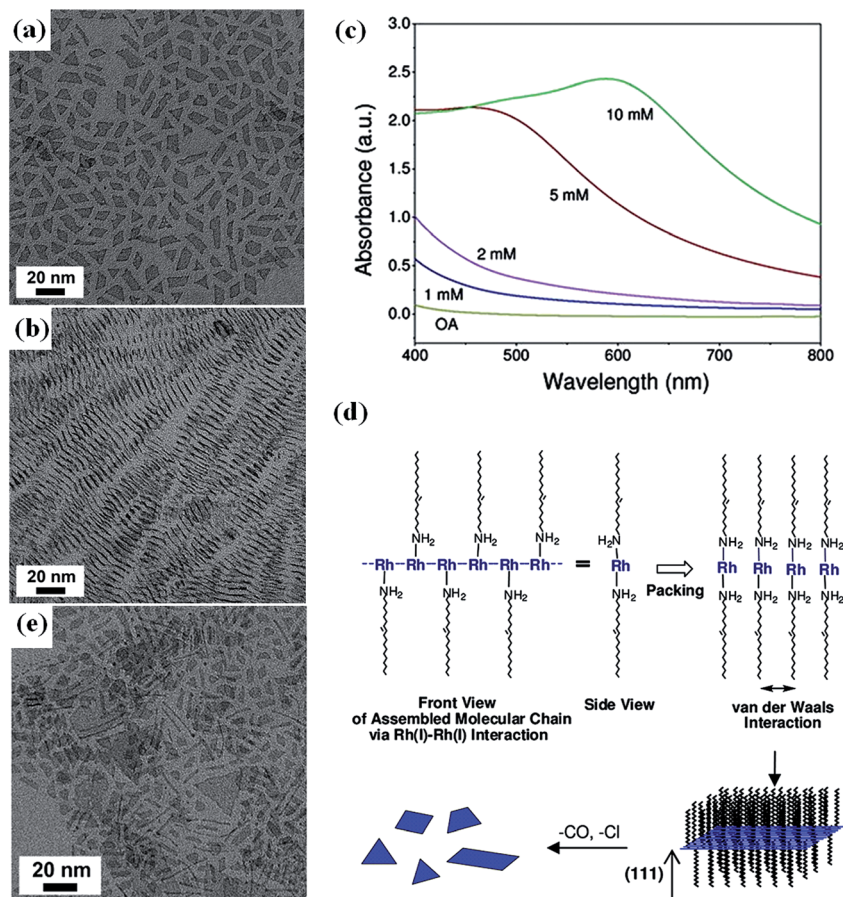


Fig. 6 (a) TEM images of individual Rh nanosheets that have 60° or 120° edges. (b) TEM images of the packing structure of Rh nanosheets, from which the thickness of the nanosheets was measured to be 1.3 ± 0.2 nm. (c) UV-Vis absorption spectra of the precursor solution, showing the broad shoulder band that indicates the Rh metal–metal interaction in the growth solution. (d) Illustration of the formation mechanism of Rh nanosheets. (e) TEM images of the Rh products obtained from using dodecylamine (a shorter molecule) instead of oleylamine as a solvent. Reproduced with permission from American Chemical Society from ref. 52, Copyright 2010.

surfactant molecules is that they can form a close-packed monolayer at the water–air or water–oil interface, known as the Langmuir–Blodgett (LB) film. Such monolayers could be a great template for growing 2D nanomaterials because the organization, interaction and chemistry of the surfactant molecules can be finely tuned, which leaves researchers plenty of room to build connections between the surfactant monolayers and the materials of interest.

Employing surfactant monolayers as templates demands a facile aqueous solution synthesis route of the target material. Among the earliest work of this strategy was when Fendler *et al.* synthesized a number of materials in the trough of a commercial LB film apparatus using different surfactant molecules or their mixtures. In the synthesis of PbS,⁵⁸ Pb(NO₃)₂ solution with a pH value of 5.8 was used in the trough as the subphase, and chloroform solutions of arachidic acid (AA) was applied to the air–subphase interface. The LB film apparatus can control the surface pressure by compressing the AA monolayer to give an area density of AA molecules of approximately 0.2 nm² per molecule. H₂S was then introduced 5 cm above the monolayer-coated aqueous Pb(NO₃)₂ solution, which led to the gradual development of PbS under the monolayer surface. As shown in

Fig. 7a, equilateral triangle-like PbS nanoplates were formed under the AA monolayer. Electron diffraction showed that the basal plane of the equilateral triangles is the (111) plane. It was proposed that the formation of (111) plane-oriented nanoplates was a result of the epitaxial growth of PbS under the AA monolayer. Synchrotron X-ray studies of AA monolayers showed that they were oriented approximately normal to the liquid surface in a hexagonal closely packed array with a lattice constant of 4.85 Å. The $d_{(110)}$ spacing of 4.20 Å (Fig. 7b) matched the Pb–Pb distance of 4.20 Å in the PbS (111) plane.

The resulting triangular plates were less than 100 nm in size; therefore, they were too small to take the morphological advantage of 2D nanomaterials. Possible reasons that prevented large-scale epitaxial growth may be the instabilities of the template and domain formation that led to local non-uniformity in the monolayer. To produce large-area 2D nanomaterials, a more robust interaction between the surfactant monolayer as a template and the material of interest needs to be realized. One idea is to choose a material system that incorporates the monolayer in the crystal structure such that the monolayer becomes an integral part of the 2D crystal growth. Using this strategy, we have developed large-area, free-standing zinc

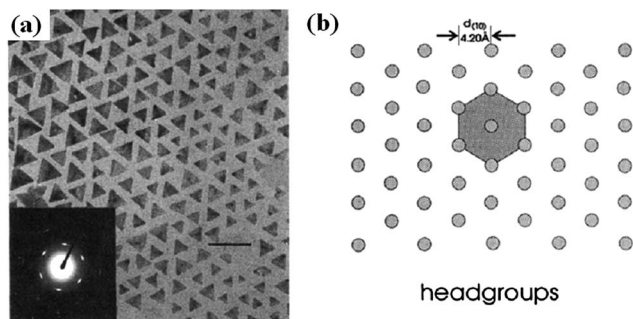


Fig. 7 (a) TEM image of triangular PbS nanoplates. The inset is the electron diffraction pattern of a single nanoplate, and the exposed surface is identified as (111). (b) Schematic illustration of the hexagonal packing of the headgroups of arachidic acid molecules on the water surface. The distance between two columns of headgroups is 4.20 nm. Reproduced with permission from American Chemical Society from ref. 58, Copyright 1995.

hydroxyl dodecylsulfate (ZHDS) nanomembranes that can cover the entire water surface.^{2,59}

$\text{Zn}(\text{NO}_3)_2$ and hexamethylenetetramine (HMTA) are commonly used precursors for 1D ZnO nanostructure growth.

However, in the presence of sulfate ions, elemental zinc and Zn^{2+} ions often mineralize to zinc hydroxyl sulfate hydrates. Therefore, the surfactant used in this work was dodecylsulfate (DS) to ensure that the sulfate headgroups would direct the nucleation and growth of ZHDS in which the DS monolayer is the starting crystallographic layer. In a typical synthesis, 25 mM $\text{Zn}(\text{NO}_3)_2$ and HMTA were used along with 20 mM sodium DS (above its critical micelle concentration), and the reactor was placed in a 90 °C convection oven for 4 hours. Fig. 8a is an image from an optical microscope where large area nanomembranes on the Si substrate are presented with a few cracks and wrinkles formed during the transfer process. The inset in Fig. 8a is a picture of the as-grown ZHDS nanomembrane, which covered the entire surface of the growth solution in a glass dish. The color contrast in Fig. 8a resulted from thickness variations. Fig. 8b is an AFM topography scan of the nanomembranes, and the thickness was measured to be 150 nm. TEM characterization revealed that the continuous ZHDS nanomembranes are composed of tens of micron-sized hexagonal single crystal plates (Fig. 8c). These single crystal plates have either a flat surface as shown in Fig. 8d or a surface with hexagonal helical contours (Fig. 8e), indicating a screw-

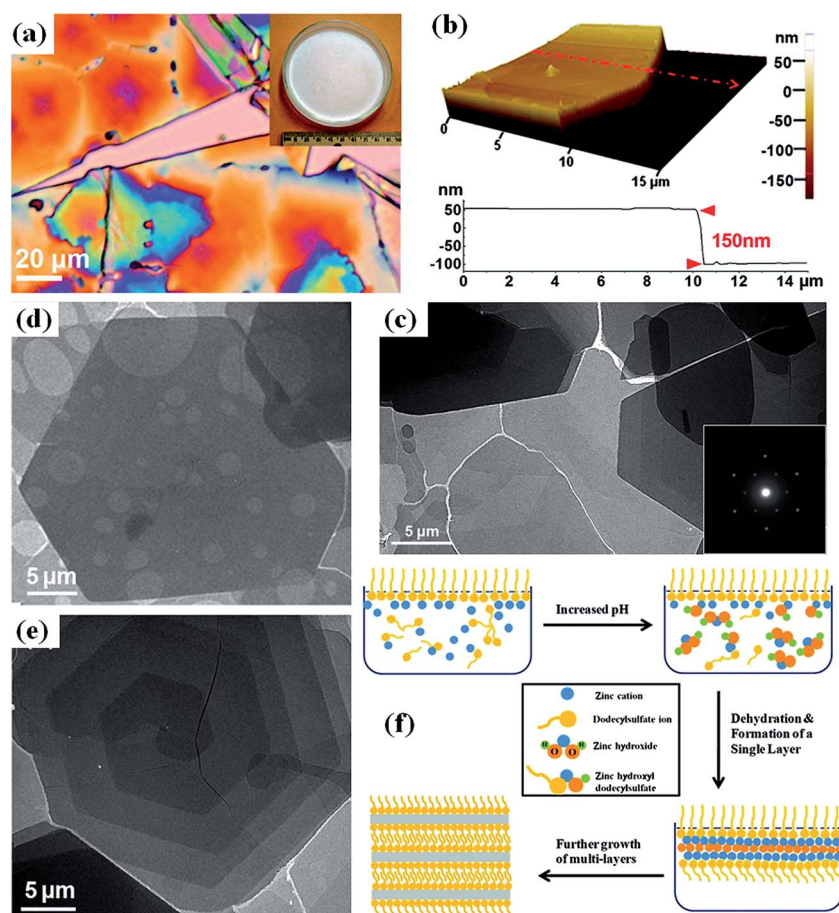


Fig. 8 (a) Optical microscopy image of the ZHDS nanomembranes. The inset is a picture of the as-grown intact nanomembranes afloat on the water surface in a glass dish. (b) AFM topography scan. (c)–(e) TEM images. (c) Single-crystal grains overlap forming a large-scale single crystal as shown by the electron diffraction pattern in the inset. (d) Flat surface on some hexagonal grains. (e) Spiral surface hillocks on other hexagonal grains. (f) Schematic illustration of the formation process of ZHDS NMs at the water surface assisted by DS ions. Reproduced with permission from American Chemical Society from ref. 59, Copyright 2012.

dislocation driven growth. Fig. 8f illustrates the schematic formation process of ZHDS nanomembranes at the water surface assisted by DS ions: DS ions form a negatively charged monolayer at the wafer surface, under which zinc cations are enriched and an electrostatic double layer is formed. As the temperature increases, the pH value of the solution, buffered by HMTA and its thermal decomposition to ammonia also increases, which initiates the crystallization of ZHDS both underneath the DS ion monolayer and in the bulk solution.

We also observed that the hexagonal single crystal grains of ZHDS experienced a phase transformation under extended reaction time (about 20 hours) and rectangular sheets were obtained.⁶⁰ Fig. 9a is an optical microscopy image of the rectangular sheets on a Si substrate. AFM topology scan revealed a film thickness from ~ 100 nm to ~ 300 nm, and some rectangular sheets exhibited conspicuous surface steps (Fig. 9b). The electron diffraction pattern (Fig. 9d) of a single rectangular sheet (see TEM image in Fig. 9c) displays orthorhombic symmetry (weak spots) within the hexagonal diffraction pattern (bright spots). The hexagonal symmetry came from the crystal structure of ZHDS, while the orthorhombic diffraction spots were identified as a long-range order of zinc vacancies forming an orthorhombic superlattice. Fig. 9e shows an illustration of the zinc vacancy superlattice with lattice constant $a' = 2a$, and

$b' = \sqrt{3}a$, where a is the Zn–Zn distance in the hexagonal ZHDS. Studies on the time evolution of the phase transformation and precursor concentration profiles indicated that the phase transformation was triggered by the formation of zinc vacancies due to limited diffusion of Zn^{2+} ions at the water–air interface and was driven by constant and sufficient supply of DS ions. Based on the observation that the phase-transformation occurred around the dislocation cores, it was also proposed that the phase-transformation occurred along the same spiral trajectory along which the initial hexagonal sheets were grown by screw dislocations. This process bore great resemblance to the classic periodic slip process that explains the polymorphism in materials such as ZnS and SiC.

Because the layered nature of ZHDS nanomembranes and the fact that the intercalated DS molecules impaired their electrical properties, it was intuitive to try to remove the DS molecules and convert the zinc hydroxyl layer to ZnO nanosheets. Based on the anionic nature of the DS ions, rectangular ZHDS sheets were added to *n*-butylamine. Fig. 9f is a TEM image of the exfoliated ZnO nanosheets, and the inset is the electron diffraction pattern that corresponds to wurtzite ZnO. A high-resolution TEM image (Fig. 9g) revealed the polycrystalline nature of the nanosheets. The thickness of the nanosheets was 4 nm or its multiples as measured by the AFM topography scan

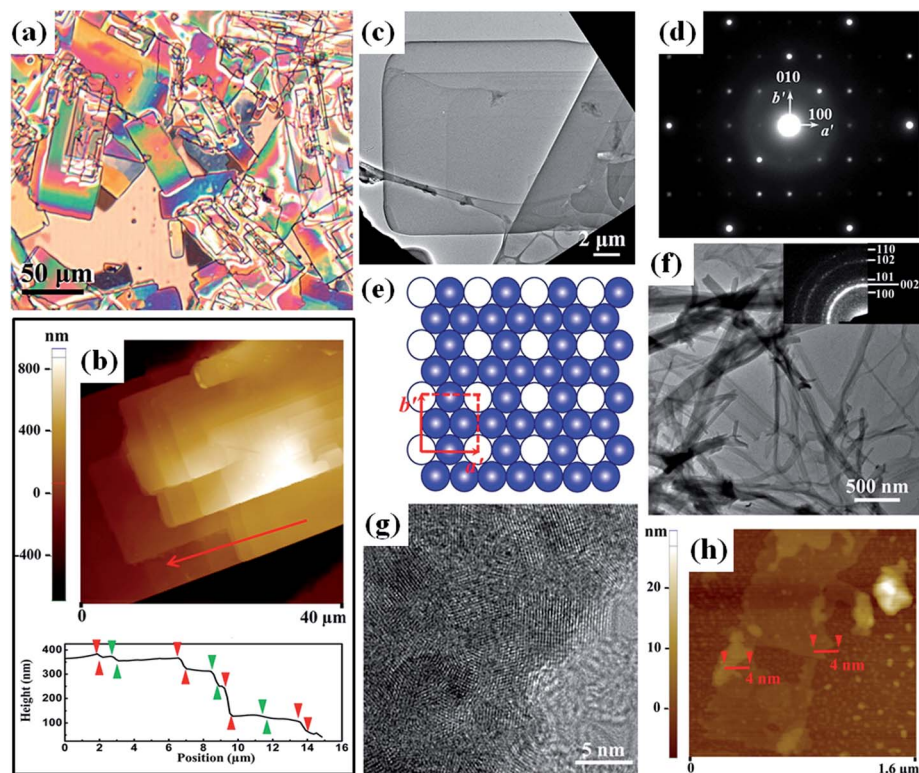


Fig. 9 (a) Optical microscopy image of the rectangular ZHDS nanosheets. (b) AFM topography scan showing the surface steps. (c) TEM image of a single rectangular nanosheet. (d) Corresponding electron diffraction pattern, in which the rhombohedral pattern is present in addition to the hexagonal pattern. (e) Schematic illustration of the superlattice of zinc vacancies. (e) and (f) TEM image of (f) exfoliated ZnO nanosheets, most of which are rolled up. The inset is a diffraction pattern showing the polycrystalline nature. (g) High-resolution image. (h) AFM topography scan of exfoliated ZnO nanosheets on a mica surface. The thickness was 4 nm or its multiples. Reproduced with permission from American Chemical Society from ref. 60, Copyright 2013.

shown in Fig. 9h. In the zinc hydroxyl layer of ZHDS, O–H groups are strongly polarized and the H atoms have a strong propensity for forming H-bonds, particularly with the N atoms on *n*-butylamine. We believe that the role of *n*-butylamine is to remove the protons from the O–H groups and form cationic amines, which subsequently remove DS ions from ZHDS. The reaction can be written as $\text{Zn}(\text{OH})_2 \cdot \text{Zn}(\text{DS})_2 + 2\text{C}_4\text{H}_{11}\text{N} \rightarrow 2\text{ZnO} + 2\text{C}_4\text{H}_{11}\text{NH}^+ \cdot \text{DS}^-$.

5. Other processes in solvothermal syntheses

We have introduced some solvothermal syntheses in the above sections when the growth mechanism can be categorized as oriented attachment, screw dislocation-driven growth, or surfactant-assisted growth. These mechanisms do not exclusively occur in solvothermal processes. In this section, we focus on solvothermal synthesis as an experimental method and discuss other processes that occur in the solvothermal growth of 2D nanomaterials. We find that thermodynamic factors, such as the relative energy among different facets, often determine the 2D geometry of the products. An important feature of solvothermal synthesis is that the autoclaves can create a high-temperature and high-pressure condition, under which water as well as other solvents exhibit significantly different chemical and physical properties, such as dissociation constant, viscosity, and dielectric constant. As a result, solubility, reactivity, and mass transport in solvothermal synthesis can be varied significantly under different system conditions.⁶¹

5.1. Metal oxide with layered crystal structure

Several metal oxides with a monoclinic structure have been synthesized in the form of nanosheets by hydrothermal methods. Lanthanide titanate ($\text{La}_2\text{Ti}_2\text{O}_7$) is one of them. A few-atomic-layer-thick $\text{La}_2\text{Ti}_2\text{O}_7$ nanosheets were synthesized hydrothermally by Li *et al.*⁶² Lanthanum nitrate and titanium sulfate were used as lanthanum and titanium precursors, respectively. As in a typical hydrothermal synthesis of metal oxide, NaOH was used and the reaction was conducted at 200 °C for 24 hours. TEM images showed that the nanosheets were in a rectangular shape and a few microns wide (Fig. 10a). It was noted that an appropriate amount of NaOH was essential to obtain $\text{La}_2\text{Ti}_2\text{O}_7$ rather than TiO_2 or $\text{La}(\text{OH})_3$. It was not discussed in this work how the $\text{La}_2\text{Ti}_2\text{O}_7$ grew in 2D, but the layered monoclinic crystal structure and the feeble bonding between layers were considered to be critical in the 2D growth. In the monoclinic crystal structure of $\text{La}_2\text{Ti}_2\text{O}_7$ (illustrated in Fig. 10b),⁶³ the layers are built from (110) perovskite slabs, with each slab containing La ions and corner-sharing TiO_6 octahedrons. Adjacent layers are staggered by half of a TiO_6 height, where the TiO_6 octahedrons are disconnected and only weakly bonded through the interaction with La ions.

First synthesized by Marchand *et al.*,⁶⁴ $\text{TiO}_2(\text{B})$ is a monoclinic polymorph of TiO_2 and has exotic properties in photocatalysis,⁶⁵ electrochemistry, and Li-ion battery applications.⁶⁶ It can be viewed as a layered structure because it has open

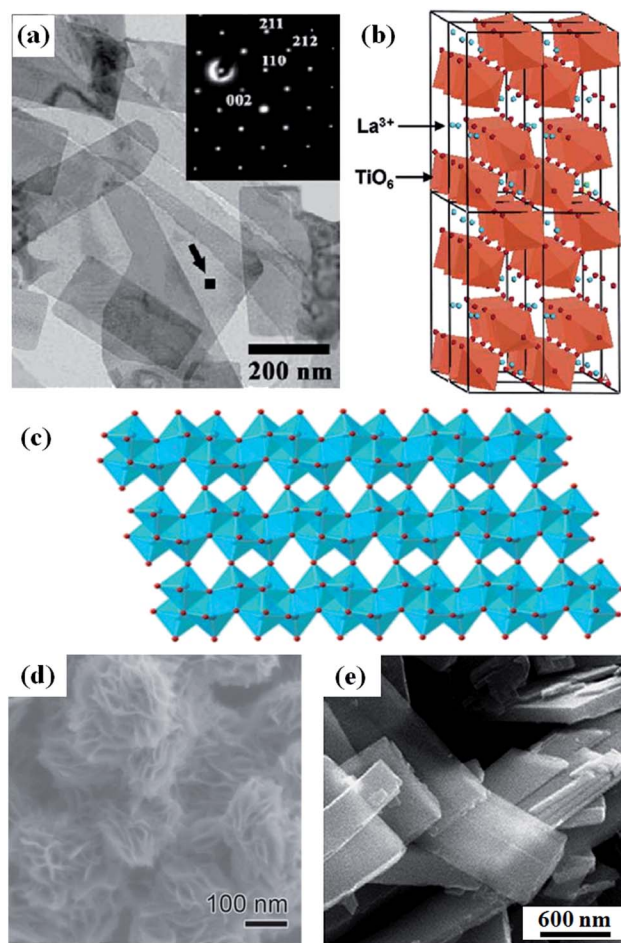


Fig. 10 (a) TEM image of $\text{La}_2\text{Ti}_2\text{O}_7$ nanosheets. The inset is the electron diffraction pattern taken from a nanosheet area labeled by the square black dot marked by the arrow. (b) Illustration of the monoclinic-layered structure of $\text{La}_2\text{Ti}_2\text{O}_7$, in which the bonding between corners of the TiO_6 octahedra is broken between layers. (c) Projection of the crystal structure of $\text{TiO}_2(\text{B})$ along the *c*-axis. (d) SEM image of the aggregates of $\text{TiO}_2(\text{B})$ nanosheets. (e) SEM image of individual $\text{VO}_2(\text{B})$ nanosheets. (a) Reproduced with permission from IOP Publishing from ref. 62, Copyright 2006. (b) Reproduced with permission from American Chemical Society from ref. 63, Copyright 2006. (c) Reproduced with permission from American Chemical Society from ref. 66, Copyright 2013. (d) Reproduced with permission from Wiley from ref. 67, Copyright 2012. (e) Reproduced with permission from Springer from ref. 68, Copyright 2005.

channels parallel to the *b*-axis. As shown in Fig. 10c, the layers are staggered and contain TiO_6 octahedra sharing their edges in-plane and sharing corners between layers. Liu *et al.* synthesized petal-like aggregates of $\text{TiO}_2(\text{B})$ nanosheets with thicknesses of 5–10 nm by the solvothermal method (Fig. 10d).⁶⁷ In their process, TiCl_4 was dissolved in ethylene glycol under stirring for 2 hours prior to adding 25% ammonium hydroxide. $\text{TiO}_2(\text{B})$ could be obtained after a 24-hour solvothermal treatment at 150 °C. The crystallinity of $\text{TiO}_2(\text{B})$ was greatly improved by calcination at 350 °C for 2 hours. The exposed surface of $\text{TiO}_2(\text{B})$ nanosheets was the (001) facet. In another synthesis of $\text{TiO}_2(\text{B})$ nanosheets by Yu *et al.*, anatase TiO_2 powder produced by calcination of $\text{Ti}(\text{OH})_4$ ethanol-gel at 500 °C was used as the

precursor, which was then added to 10 M NaOH solution and treated hydrothermally at 200 °C for 72 hours.⁶⁸ Similar to Liu *et al.*'s work, the hydrothermal treatment yielded amorphous nanosheets, which were topotactically transformed to TiO₂(B) nanosheets by rinsing with HCl for 30 min in a supersonic batch and calcinating at 500 °C. As a structural analog of TiO₂(B), petal-like aggregates of VO₂(B) nanosheets were also synthesized by the hydrothermal method, in which ammonium vanadate was used as the precursor and the reaction was conducted at 180 °C for 72 hours.⁶⁹ In another synthesis by Whitaker *et al.*, in which V₂O₅ was used as the precursor along with ethanol or acetone as the reducing agent, ~100 nm thick individual single crystal rectangular nanosheets were obtained (Fig. 10e).⁷⁰ The hydrothermal treatment in this synthesis was conducted at 210 °C for 72 hours.

In these examples of TiO₂(B) and VO₂(B) nanosheets, as well as La₂Ti₂O₇ nanosheets, no surfactant was used. Comparing the crystal structure of the materials and the hydrothermal reaction conditions in these examples, we find that there is an intrinsic driving force for the formation of nanosheets of layered, monoclinic materials, although the kinetic mechanism of the 2D growth in these examples is still unknown (be it oriented attachment, screw-dislocation growth, or layer-by-layer growth). This makes sense given the fact that the surface of individual layers is more stable than the edges which are under-coordinated and thermodynamically unfavorable.⁷¹ One may argue that there are a number of reports where TiO₂(B) and VO₂(B) can also be hydrothermally synthesized in a 1D form without surfactants; however, they are often grown indirectly and a conversion from other polymorphs is needed. For example, anatase TiO₂ or metal (Na or K) titanate hydroxide (*e.g.* Na_xH_{2-x}Ti₃O₇) nanowires/nanotubes were often found to have formed first hydrothermally before being converted into TiO₂(B) through acid wash and thermal calcination.⁷²⁻⁷⁵ In the light of precursor selection for both TiO₂(B) and VO₂(B), when a soluble precursor is used, aggregates of smaller nanosheets were obtained, whereas when a solid oxide was used, the products were larger individual nanosheets. Therefore, the state of precursors should have a great influence on the growth mechanism, possibly through the control of intermediate species that finally crystallize into the nanosheet materials.

A number of other solvothermal and non-solvothermal syntheses also indicate that there is an intrinsic driving force to the formation of nanosheets of layered crystals with monoclinic and other symmetries. BiOCl has a layered tetragonal structure in which Bi₂O₂ slabs are interleaved by double slabs of Cl atoms in the tetragonal matlockite structure. Ye *et al.* reported the synthesis of BiOCl nanosheets by a non-solvothermal method.⁷⁶ In their synthesis, BiCl₃ was dissolved in ethanol, and thiourea (Tu) was added slowly to form Bi_n(Tu)_xCl_{3n} molecular precursors. BiOCl nanosheets were obtained 20 minutes after adding this precursor to deionized water under sonication. The exposed facets are (001), similar to BiOCl nanoplates reported by Geng *et al.* and Lei *et al.*^{77,78} Through a solvothermal method using Bi(NO₃)₃ as the Bi precursor and NaOH as the mineralizer, BiOBr nanosheets were synthesized by Lin *et al.* where KBr was used to provide the halide ions.⁷⁹ Moreover, BiOCl and BiOBr

nanobelts with the exposed (001) facets were synthesized by Deng *et al.* by using CTAC (cetyltrimethylammonium chloride) and CTAB, respectively.⁸⁰

5.2. Dissolution–recrystallization process in solvothermal method

Crystal growth from solution is essentially a precipitation process, which involves dynamic dissolution–recrystallization processes. The classic Ostwald ripening process, in which the difference between the solubility of small and large nanoparticles leads to a defocusing in particle size (*i.e.* big nanoparticles grow even bigger at the expense of smaller particles), is a perfect example of this dissolution–recrystallization process. Another consequence of dynamic dissolution–recrystallization is spontaneous phase transformation from kinetic products to thermodynamic products and morphology evolution during the crystal growth in solution. In fact, crystal growth in solution often starts with a thermodynamically unstable phase, followed by a phase transformation to thermodynamically stable phases. This is referred to as the Ostwald's rule of stages.^{81,82} Similarly, crystal growth can also start with a thermodynamically unstable morphology due to kinetics, and then recrystallize to a thermodynamically stable morphology. In the case of the solution synthesis of 2D nanomaterials, 2D morphology can be transformed from other morphologies after an extended reaction time.

Yang *et al.* synthesized β-Co(OH)₂ and Co₃O₄ nanosheets by the hydrothermal method.^{83,84} β-Co(OH)₂ nanosheets were synthesized on a nickel foam by using Co(NO₃)₂·6H₂O as the Co precursor, and NH₄F along with urea as the mineralizer. To obtain Co₃O₄ nanosheets, the Co(OH)₂ nanosheets were loaded in the Teflon-lined stainless steel autoclave again with the addition of Co²⁺ salts and a base (urea or HMT). This secondary hydrothermal treatment was considered a coordinating etching and recrystallization process. The excess urea or HMT introduced to the solution was able to coordinate the etching of Co(OH)₂ by forming a soluble complex and releasing OH⁻ ions to facilitate the recrystallization. The addition of Co²⁺ salt should help the recrystallization too. Fig. 11a–e show the morphology evolution from β-Co(OH)₂ to Co₃O₄ before ((a), β-Co(OH)₂) and during the secondary hydrothermal treatment at 3, 6, 9, and 12 hours, respectively. The β-Co(OH)₂ nanosheets were quite thick (about 200 nm). After 3 hours, the nanosheets were significantly thinner, indicating the dissolution of β-Co(OH)₂, and Co₃O₄ nanowires started to grow on the surfaces of the nanosheets. The β-Co(OH)₂ nanosheets disappeared almost completely by 6 hours (c). Then, these nanowires were grown into Co₃O₄ nanosheets after 9 hours (d), and finally they evolved into nanosheets with better crystallinity and well-defined surface and edge facets (e).

Zhao *et al.* reported the hydrothermal synthesis of metastable phase FeVO₄-II nanosheets (orthorhombic) with exposed (010) facets.⁸⁵ The obtained nanosheets were rectangular and were ~50 nm thick and a few microns in size. The growth solution contained equal amounts of FeCl₃ and NH₄VO₃, and the pH value was adjusted to 3. Unlike the synthesis of BiVO₄ that was introduced in Section 4.1, no surfactant was used in

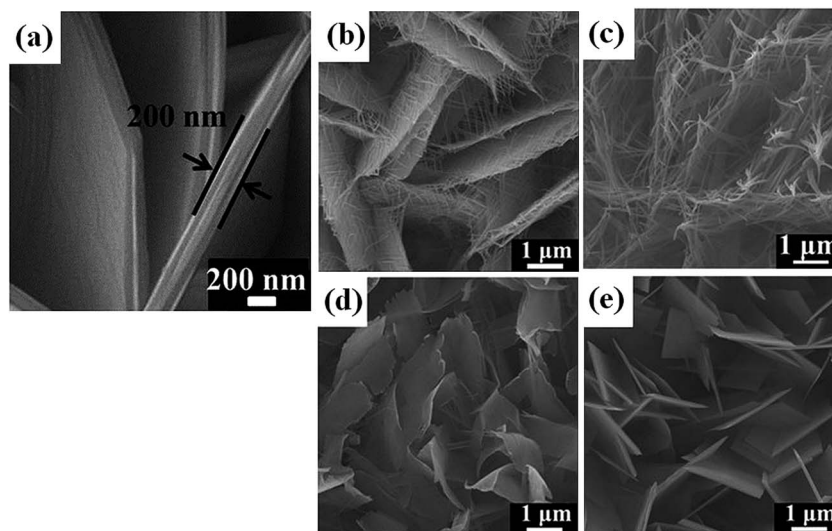


Fig. 11 SEM image of (a) β -Co(OH) $_2$ nanosheet. (b)–(e) Co_3O_4 nanowires/nanosheets obtained by the hydrothermal treatment of β -Co(OH) $_2$ nanosheets for 3, 6, 9, and 12 hours, respectively. Reproduced with permission from Nature Publishing Group from ref. 84, Copyright 2013.

this synthesis. The hydrothermal treatment was conducted at 180 °C for 24 hours. Temperature was found to be very crucial in obtaining the FeVO $_4$ -II phase. Lowering the temperature to 150 °C produced triclinic FeVO $_4$ -I. The mechanism of the 2D growth was not discussed. However, we believe that this could be another example of nanosheets produced from dissolution–recrystallization. It is possible that rectangular nanosheets were the thermodynamically stable phase and morphology under the hydrothermal conditions, because products sampled at different reaction times showed that sheaves of nanorods were formed prior to the formation of nanosheets starting at 24 hours.

The dissolution–recrystallization process is ubiquitous in the solution growth of crystals. When other growth mechanisms are dominant, such as oriented attachment or dislocation-driven growth, it can modify the surface morphology of the grown 2D nanomaterials. When the modification of surface morphology by dissolution–recrystallization becomes significant, it can also overwhelm the footprints of the initial growth mechanism, which often renders difficulty in the identification of the initial growth mechanisms. For example, the surface helical hillocks sometimes are not observable even if the 2D crystal grown was driven by screw dislocations.

5.3. The use of PVP and mixed solvents

A number of ultrathin metal nanoplates have also been synthesized by hydrothermal/solvothermal methods. Yin *et al.* reported the hydrothermal synthesis of triangular Ru nanosheets with the edge length from 15 to 30 nm and the thickness between 2 to 4 nm (Fig. 12a).⁸⁶ In their synthesis, RuCl $_3 \cdot x\text{H}_2\text{O}$ was used as Ru precursor, HCHO was used as the reducing agent, and poly(vinylpyrrolidone) (PVP) was also added to the initial solution. The reaction was performed at 160 °C for 4 hours. The exposed facets were determined to be Ru (0001), and the authors ascribed the formation of 2D nanoplates to the

lower surface energy of Ru (0001), which is 0.96 and 0.33 J m $^{-2}$ lower than that of Ru (10 $\bar{1}$ 0) $_a$ and Ru(10 $\bar{1}$ 0) $_b$, respectively, as suggested by their DFT calculations. They also discussed that PVP should have no significant facet-selective adsorption effects on small nanocrystals. Experimentally, a change in the amount or molecular weight of PVP did not make any obvious difference in the morphology of Ru nanoplates. Duan *et al.* synthesized Rh nanosheets with an edge length of 500 to 600 nm by a solvothermal method, as shown in Fig. 12b.⁸⁷ Rh(III) acetylacetonate and PVP were dissolved in a mixed solvent that consisted of equal volumes of benzyl alcohol and formaldehyde. The reaction was conducted at 180 °C for 8 hours. FTIR and energy-dispersive X-ray (EDX) spectra indicated that the Rh nanosheets were capped with PVP. A comparison between the kinematical electron diffraction pattern with simulated patterns of single, double, and triple layers of Rh revealed that the Rh nanosheets were only a single layer of hexagonal Ru atoms. In control experiments when L-ascorbic acid was added together with PVP and benzyl alcohol was used as the sole solvent, only PVP-capped Rh nanoparticles were obtained. PVP were used in both of the above syntheses; however, preferential adsorption of PVP on different facets may not be necessary in the cases here. Like the synthesis of Pd nanosheets in Section 3.1, the role of PVP might only be to stabilize the nanosheets from aggregation.

Rangappa *et al.* synthesized Li $_2$ FeSiO $_4$ and Li $_2$ MnSiO $_4$ nanosheets by a solvothermal method using water and ethanol mixed solvent.⁸⁸ Fig. 12c shows a TEM image of Li $_2$ FeSiO $_4$ nanosheets. AFM measurement of individual nanosheets revealed an average thickness of 3 nm. Compared to the common practice in the synthesis of Li $_2$ MSiO $_4$ (M = Fe or Mn), in which the reaction temperature is generally below 200 °C,^{89,90} their synthesis of Li $_2$ MSiO $_4$ nanosheets features high-temperature and mixed solvents. At 400 °C, the reaction is in a supercritical condition as pointed out by the authors. The effect of ethanol-to-water ratio was also presented. When

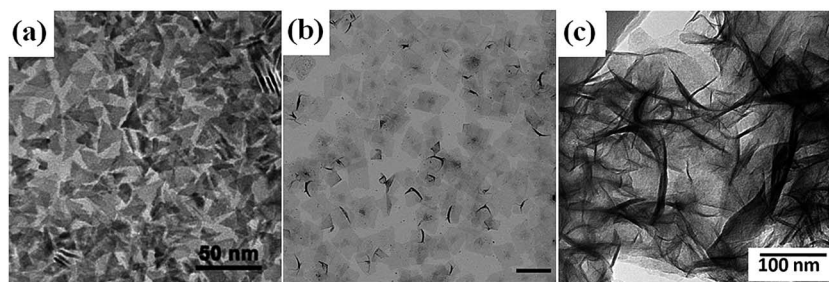


Fig. 12 TEM image of (a) Ru nanosheets. (b) Rh nanosheets, scale bar = 1 μm . (c) $\text{Li}_2\text{FeSiO}_4$ nanosheets. (a) and (c) Reproduced with permission from American Chemical Society from ref. 86 and 88, respectively, Copyright 2012. (b) Reproduced with permission from Nature Publishing Group from ref. 87, Copyright 2014.

ethanol-water = 1 : 1, only spherical and cubic nanoparticles were obtained; moreover, at a 3 : 1 ratio, nanosheets were formed. Ostwald ripening and oriented attachment were proposed for the formation of these nanosheets, although adequate investigations were not provided.

6. Outlook for the synthesis design and applications of 2D nanomaterials

To explore more scientific and technology opportunities from 2D nanomaterials, more effort should be placed on optimizing their morphology (area and thickness) and developing a wider range of 2D materials. We have separately reviewed different mechanisms that could lead to 2D crystal growth, including oriented attachment, screw dislocation-driven growth, surfactant-assisted synthesis, and solvothermal synthesis. It should be noted that these mechanisms are often operative simultaneously. For instance, the adsorption of surfactants, including chemical bonding on crystal facets, often plays a critical role in directing the dimension of oriented attachment, and in modifying the growth velocity at screw dislocation steps. The dissolution–recrystallization process is perennial throughout the nucleation and growth process of crystals and can modify the morphology of crystals grown by oriented attachment or screw dislocations. One has to comprehensively consider all these aspects in designing the synthesis of 2D nanomaterials and optimizing their morphology. We also introduced the surfactant monolayer-guided approach to large-area free-standing nanomembranes. Tailoring this approach and applying it to self-assembled monolayers (SAMs) on substrates could also be fruitful.

The crystal structure of the synthesized 2D materials also plays an important role in considering the growth mechanism for the design of experiments. In 2D-oriented attachment, the materials are often of higher crystal symmetry, such as cubic structure in PbS and CeO_2 , where many facets are crystallographically equivalent. Surfactants can be used to protect some equivalent facets while allowing oriented attachment between other equivalent facets such that oriented attachment can be very directional and 2D materials can be produced. TiO_2 and SnO_2 are two materials for which oriented attachment is extensively studied. They can have different tetragonal

polymorphs, including anatase and rutile. In these crystal structures with lower symmetry, spontaneous oriented attachment does not necessarily result in 2D materials. 2D screw dislocation-driven growth often occurs in screw dislocation-prone materials, and these materials are often hexagonal or pseudohexagonal, as in the case of ZHS and CuGaO_2 . As discussed in Section 5.1, crystals with layered structures and monoclinic crystal symmetry can be synthesized directly into nanosheets with or without surfactants.

To unleash the application potential of 2D nanomaterials, it is important to take the advantage of their 2D geometry. While research interest in exfoliated 2D materials is often placed on the electronic properties, solution-grown 2D materials exhibit their unique properties through their large surface area and specific exposed facets in electrochemical and catalytic applications. First of all, 2D nanomaterials are often only a few nanometers thick or even thinner, providing a large surface-to-volume ratio. This is beneficial for applications where the general surface area plays a vital role in device performance, such as supercapacitors and batteries.^{91–95} Secondly, 2D nanomaterials provide an overwhelming percentage of one specific crystal facet. Different crystal facets have dissimilar electronic structures. They have profound effects on the charge transfer and the kinetics of chemical reactions.^{96,97} Therefore, the exposed facet of nanosheets should be engineered to best suit for the specific requirements of catalysis^{48,86,98} and photochemical applications.^{99–102} The exposed facets of exfoliated 2D materials are often chemically inert, and the less exposed side surfaces around the edge are active.¹⁰³ In comparison, the exposed facets of solution-grown 2D materials can be controlled by the synthesis design. In order to expose the active facets that can often be thermodynamically unfavorable, the adsorbed species on the target crystal facets should be rationally designed to screen the target facets from either growth or oriented attachment. These adsorbed species should ideally be able to be removed. Thirdly, there exists a wide array of mature fabrication and processing techniques for thin films, borrowed from the well-established semiconductor device industry, for making quick use of novel 2D materials. To date, industry's inexperience with both 0D and 1D material geometries has resulted in the chronic, unsuccessful leveraging of these form factors in conventional device applications. While this advantage of 2D geometry is true for macroscopic nanomembranes, the

assembly and fabrication of microscopic nanoplates and nanosheets into electronic and optoelectronic devices remains challenging. Lastly, although the mechanical flexibility of 2D nanomaterials have unlocked their applications in flexible electronics and conformal biomedical devices, other aspects of their mechanical properties have not yet been investigated and utilized extensively.¹⁰⁴ We have demonstrated that rectangular ZHDS nanosheets behave like structural polymers in nano-indentation experiments.⁶⁰ However, more effort should be placed on exploring the application implication of the mechanical properties of 2D nanomaterials.^{105,106}

Acknowledgements

The authors acknowledge the financial support from Air Force under Award FA9550-13-1-0168 and National Science Foundation under Award CMMI-1148919.

References

- C. N. R. Rao, A. K. Sood, K. S. Subrahmanyam and A. Govindaraj, *Angew. Chem., Int. Ed.*, 2009, **48**, 7752.
- B. Nikoobakht and X. Li, *ACS Nano*, 2012, **6**, 1883.
- F. Bonaccorso, Z. Sun, T. Hasan and A. C. Ferrari, *Nat. Photonics*, 2010, **4**, 611.
- Q. H. Wang, K. Kalantar-Zadeh, A. Kis, J. N. Coleman and M. S. Strano, *Nat. Nanotechnol.*, 2012, **7**, 699.
- B. Radisavljevic, A. Radenovic, J. Brivio, V. Giacometti and A. Kis, *Nat. Nanotechnol.*, 2011, **6**, 147.
- J. A. Rogers, M. G. Lagally and R. G. Nuzzo, *Nature*, 2011, **477**, 45.
- I. Monch, J. Schumann, M. Stockmann, K. F. Arndt and O. G. Schmidt, *Smart Mater. Struct.*, 2011, **20**, 085016.
- M. H. Huang, F. Cavallo, F. Liu and M. G. Lagally, *Nanoscale*, 2011, **3**, 96.
- G. Eda, G. Fanchini and M. Chhowalla, *Nat. Nanotechnol.*, 2008, **3**, 270.
- S. I. Park, Y. J. Xiong, R. H. Kim, P. Elvikis, M. Meitl, D. H. Kim, J. Wu, J. Yoon, C. J. Yu, Z. J. Liu, Y. G. Huang, K. Hwang, P. Ferreira, X. L. Li, K. Choquette and J. A. Rogers, *Science*, 2009, **325**, 977.
- V. P. Verma, S. Das, I. Lahiri and W. Choi, *Appl. Phys. Lett.*, 2010, **96**, 203108.
- H. C. Yuan, G. K. Celler and Z. Q. Ma, *J. Appl. Phys.*, 2007, **102**, 034501.
- R. H. Kim, D. H. Kim, J. L. Xiao, B. H. Kim, S. I. Park, B. Panilaitis, R. Ghaffari, J. M. Yao, M. Li, Z. J. Liu, V. Malyarchuk, D. G. Kim, A. P. Le, R. G. Nuzzo, D. L. Kaplan, F. G. Omenetto, Y. G. Huang, Z. Kang and J. A. Rogers, *Nat. Mater.*, 2010, **9**, 929.
- J. Viventi, D. H. Kim, J. D. Moss, Y. S. Kim, J. A. Blanco, N. Annetta, A. Hicks, J. L. Xiao, Y. G. Huang, D. J. Callans, J. A. Rogers and B. Litt, *Sci. Transl. Med.*, 2010, **2**, 24ra22.
- J. Yoon, S. Jo, I. S. Chun, I. Jung, H. S. Kim, M. Meitl, E. Menard, X. L. Li, J. J. Coleman, U. Paik and J. A. Rogers, *Nature*, 2010, **465**, 329.
- M. Naguib, M. Kurtoglu, V. Presser, J. Lu, J. J. Niu, M. Heon, L. Hultman, Y. Gogotsi and M. W. Barsoum, *Adv. Mater.*, 2011, **23**, 4248.
- H. S. S. R. Matte, A. Gomathi, A. K. Manna, D. J. Late, R. Datta, S. K. Pati and C. N. R. Rao, *Angew. Chem., Int. Ed.*, 2010, **49**, 4059.
- R. S. Wagner and W. C. Ellis, *Appl. Phys. Lett.*, 1964, **4**, 89.
- A. I. Persson, M. W. Larsson, S. Stenstrom, B. J. Ohlsson, L. Samuelson and L. R. Wallenberg, *Nat. Mater.*, 2004, **3**, 677.
- T. J. Trentler, K. M. Hickman, S. C. Goel, A. M. Viano, P. C. Gibbons and W. E. Buhro, *Science*, 1995, **270**, 1791.
- J. D. Holmes, K. P. Johnston, R. C. Doty and B. A. Korgel, *Science*, 2000, **287**, 1471.
- S. A. Morin, M. J. Bierman, J. Tong and S. Jin, *Science*, 2010, **328**, 476.
- F. Meng, S. A. Morin, A. Forticaux and S. Jin, *Acc. Chem. Res.*, 2013, **46**, 1616.
- X. D. Zhang and Y. Xie, *Chem. Soc. Rev.*, 2013, **42**, 8187.
- C. J. Dalmaschio, C. Ribeiro and E. R. Leite, *Nanoscale*, 2010, **2**, 2336.
- J. Zhang, F. Huang and Z. Lin, *Nanoscale*, 2010, **2**, 18.
- N. D. Burrows, V. M. Yuwono and R. L. Penn, *MRS Bull.*, 2010, **35**, 133.
- D. S. Li, M. H. Nielsen, J. R. I. Lee, C. Frandsen, J. F. Banfield and J. J. De Yoreo, *Science*, 2012, **336**, 1014.
- Z. Y. Tang, N. A. Kotov and M. Giersig, *Science*, 2002, **297**, 237.
- C. Pacholski, A. Kornowski and H. Weller, *Angew. Chem., Int. Ed.*, 2002, **41**, 1188.
- K. S. Cho, D. V. Talapin, W. Gaschler and C. B. Murray, *J. Am. Chem. Soc.*, 2005, **127**, 7140.
- C. Schliehe, B. H. Juarez, M. Pelletier, S. Jander, D. Greshnykh, M. Nagel, A. Meyer, S. Foerster, A. Kornowski, C. Klinke and H. Weller, *Science*, 2010, **329**, 550.
- H. L. Zhu and R. S. Averbach, *Philos. Mag. Lett.*, 1996, **73**, 27.
- T. Yu, B. Lim and Y. N. Xia, *Angew. Chem., Int. Ed.*, 2010, **49**, 4484.
- S. L. Shen, J. Zhuang, X. X. Xu, A. Nisar, S. Hu and X. Wang, *Inorg. Chem.*, 2009, **48**, 5117.
- C. Wang, G. H. Du, K. Stahl, H. X. Huang, Y. J. Zhong and J. Z. Jiang, *J. Phys. Chem. C*, 2012, **116**, 4000.
- Y. Li, Y. Q. Guo, R. Q. Tan, P. Cui, Y. Li and W. J. Song, *Mater. Lett.*, 2009, **63**, 2085.
- C. Ribeiro, E. Longo and E. R. Leite, *Appl. Phys. Lett.*, 2007, **91**, 103105.
- F. Meng and S. Jin, *Nano Lett.*, 2012, **12**, 234.
- Y. G. Li and Y. Y. Wu, *Chem. Mater.*, 2010, **22**, 5537.
- S. A. Morin, A. Forticaux, M. J. Bierman and S. Jin, *Nano Lett.*, 2011, **11**, 4449.
- R. Srinivasan, B. Chavillon, C. Doussier-Brochard, L. Cario, M. Paris, E. Gautron, P. Deniard, F. Odobel and S. Jobic, *J. Mater. Chem.*, 2008, **18**, 5647.
- A. Forticaux, S. Hacialioglu, J. P. DeGrave, R. Dziedzic and J. Song, *ACS Nano*, 2013, **7**, 9.

- 44 B. Viswanath, P. Kundu, B. Mukherjee and N. Ravishankar, *Nanotechnology*, 2008, **19**, 195603.
- 45 E. J. W. Crossland, N. Noel, V. Sivaram, T. Leijtens, J. A. Alexander-Webber and H. J. Snaith, *Nature*, 2013, **495**, 215.
- 46 W. Y. Li, P. H. C. Camargo, X. M. Lu and Y. N. Xia, *Nano Lett.*, 2009, **9**, 485.
- 47 L. H. Pei, K. Mori and M. Adachi, *Langmuir*, 2004, **20**, 7837.
- 48 X. Q. Huang, S. H. Tang, X. L. Mu, Y. Dai, G. X. Chen, Z. Y. Zhou, F. X. Ruan, Z. L. Yang and N. F. Zheng, *Nat. Nanotechnol.*, 2011, **6**, 28.
- 49 L. Zhang, D. R. Chen and X. L. Jiao, *J. Phys. Chem. B*, 2006, **110**, 2668.
- 50 A. P. Zhang, J. Z. Zhang, N. Y. Cui, X. Y. Tie, Y. W. An and L. J. Li, *J. Mol. Catal. A: Chem.*, 2009, **304**, 28.
- 51 H. B. Li, G. C. Liu, S. G. Chen, Q. C. Liu and W. M. Lu, *Phys. E*, 2011, **43**, 1323.
- 52 K. Jang, H. J. Kim and S. U. Son, *Chem. Mater.*, 2010, **22**, 1273.
- 53 Z. Miao, D. S. Xu, J. H. Ouyang, G. L. Guo, X. S. Zhao and Y. Q. Tang, *Nano Lett.*, 2002, **2**, 717.
- 54 Y. K. Zhou, C. M. Shen and H. L. Li, *Solid State Ionics*, 2002, **146**, 81.
- 55 J. L. Zhang and G. Y. Hong, *J. Solid State Chem.*, 2004, **177**, 1292.
- 56 W. T. Bi, M. Zhou, Z. Y. Ma, H. Y. Zhang, J. B. Yu and Y. Xie, *Chem. Commun.*, 2012, **48**, 9162.
- 57 X. Huang, S. Z. Li, Y. Z. Huang, S. X. Wu, X. Z. Zhou, S. Z. Li, C. L. Gan, F. Boey, C. A. Mirkin and H. Zhang, *Nat. Commun.*, 2011, **2**, 292.
- 58 J. P. Yang and J. H. Fendler, *J. Phys. Chem.*, 1995, **99**, 5505.
- 59 F. Wang, J. H. Seo, Z. Q. Ma and X. D. Wang, *ACS Nano*, 2012, **6**, 2602.
- 60 F. Wang, J. E. Jakes, D. L. Geng and X. D. Wang, *ACS Nano*, 2013, **7**, 6007.
- 61 A. Rabenau, *Angew. Chem., Int. Ed.*, 1985, **24**, 1026.
- 62 K. Li, Y. Wang, H. Wang, M. K. Zhu and H. Yan, *Nanotechnology*, 2006, **17**, 4863.
- 63 R. Abe, M. Higashi, K. Sayama, Y. Abe and H. Sugihara, *J. Phys. Chem. B*, 2006, **110**, 2219.
- 64 R. Marchand, L. Brohan and M. Tournoux, *Mater. Res. Bull.*, 1980, **15**, 1129.
- 65 D. J. Yang, H. W. Liu, Z. F. Zheng, Y. Yuan, J. C. Zhao, E. R. Waclawik, X. B. Ke and H. Y. Zhu, *J. Am. Chem. Soc.*, 2009, **131**, 17885.
- 66 A. G. Dylla, G. Henkelman and K. J. Stevenson, *Acc. Chem. Res.*, 2013, **46**, 1104.
- 67 S. H. Liu, H. P. Jia, L. Han, J. L. Wang, P. F. Gao, D. D. Xu, J. Yang and S. N. Che, *Adv. Mater.*, 2012, **24**, 3201.
- 68 Y. Wu and B. Q. Xu, *Chin. Sci. Bull.*, 2005, **50**, 2153.
- 69 C. Nethravathi, C. R. Rajamathi, M. Rajamathi, U. K. Gautam, X. Wang, D. Golberg and Y. Bando, *ACS Appl. Mater. Interfaces*, 2013, **5**, 2708.
- 70 L. Whittaker, H. Zhang and S. Banerjee, *J. Mater. Chem.*, 2009, **19**, 2968.
- 71 R. Tenne and M. Redlich, *Chem. Soc. Rev.*, 2010, **39**, 1423.
- 72 B. Liu, A. Khare and E. S. Aydil, *ACS Appl. Mater. Interfaces*, 2011, **3**, 4444.
- 73 J. M. Li, W. Wan, H. H. Zhou, J. J. Li and D. S. Xu, *Chem. Commun.*, 2011, **47**, 3439.
- 74 A. R. Armstrong, G. Armstrong, J. Canales, R. Garcia and P. G. Bruce, *Adv. Mater.*, 2005, **17**, 862.
- 75 A. R. Armstrong, G. Armstrong, J. Canales and P. G. Bruce, *Angew. Chem., Int. Ed.*, 2004, **43**, 2286.
- 76 L. Q. Ye, L. Zan, L. H. Tian, T. Y. Peng and J. J. Zhang, *Chem. Commun.*, 2011, **47**, 6951.
- 77 J. Geng, W. H. Hou, Y. N. Lv, J. J. Zhu and H. Y. Chen, *Inorg. Chem.*, 2005, **44**, 8503.
- 78 Y. Q. Lei, G. H. Wang, S. Y. Song, W. Q. Fan and H. J. Zhang, *CrystEngComm*, 2009, **11**, 1857.
- 79 W. Lin, X. Wang, Y. Wang, J. Zhang, L. Zhang, B. Zhang and F. Huang, *Chem. Commun.*, 2013, DOI: 10.1039/c3cc41498a.
- 80 H. Deng, J. W. Wang, Q. Peng, X. Wang and Y. D. Li, *Chem. – Eur. J.*, 2005, **11**, 6519.
- 81 T. P. Feenstra and P. L. Debruyne, *J. Colloid Interface Sci.*, 1981, **84**, 66.
- 82 J. Nyvlt, *Cryst. Res. Technol.*, 1995, **30**, 443.
- 83 Q. Yang, Z. Y. Lu, Z. Chang, W. Zhu, J. Q. Sun, J. F. Liu, X. M. Sun and X. Duan, *RSC Adv.*, 2012, **2**, 1663.
- 84 Q. Yang, Z. Y. Lu, X. M. Sun and J. F. Liu, *Sci. Rep.*, 2013, **3**, 3537.
- 85 Y. Zhao, K. Yao, Q. Cai, Z. J. Shi, M. Q. Sheng, H. Y. Lin and M. W. Shao, *CrystEngComm*, 2014, **16**, 270.
- 86 A. X. Yin, W. C. Liu, J. Ke, W. Zhu, J. Gu, Y. W. Zhang and C. H. Yan, *J. Am. Chem. Soc.*, 2012, **134**, 20479.
- 87 H. Duan, N. Yan, R. Yu, C. R. Chang, G. Zhou, H. S. Hu, H. Rong, Z. Niu, J. Mao, H. Asakura, T. Tanaka, P. J. Dyson, J. Li and Y. Li, *Nat. Commun.*, 2014, **5**, 3093.
- 88 D. Rangappa, K. D. Murukanahally, T. Tomai, A. Unemoto and I. Honma, *Nano Lett.*, 2012, **12**, 1146.
- 89 M. Zhang, Q. P. Chen, Z. X. Xi, Y. G. Hou and Q. L. Chen, *J. Mater. Sci.*, 2012, **47**, 2328.
- 90 D. C. Xiao, L. Y. Shao, R. Ma, M. Shui, J. Q. Gao, F. T. Huang, K. Q. Wu, S. S. Qian, D. J. Wang, N. B. Long, Y. L. Ren and J. Shu, *Int. J. Electrochem. Sci.*, 2013, **8**, 7581.
- 91 J. Du, G. Zhou, H. M. Zhang, C. Cheng, J. M. Ma, W. F. Wei, L. B. Chen and T. H. Wang, *ACS Appl. Mater. Interfaces*, 2013, **5**, 7405.
- 92 L.-H. Gan, D. Deng, Y. Zhang, G. Li, X. Wang, L. Jiang and C.-R. Wang, *J. Mater. Chem. A*, 2014, **2**, 2461.
- 93 J. S. Chen, L. A. Archer and X. W. Lou, *J. Mater. Chem.*, 2011, **21**, 9912.
- 94 J. Feng, X. Sun, C. Z. Wu, L. L. Peng, C. W. Lin, S. L. Hu, J. L. Yang and Y. Xie, *J. Am. Chem. Soc.*, 2011, **133**, 17832.
- 95 H. Chen, L. Hu, M. Chen, Y. Yan and L. Wu, *Adv. Funct. Mater.*, 2013, **23**, 934.
- 96 M. Sun, S. J. Xiong, X. L. Wu, C. Y. He, T. H. Li and P. K. Chu, *Adv. Mater.*, 2013, **25**, 2035.
- 97 W. J. Ong, L. L. Tan, S. P. Chai, S. T. Yong and A. R. Mohamed, *Nanoscale*, 2014, **6**, 1946.
- 98 Q. Liu, D. Wu, Y. Zhou, H. Su, R. Wang, C. Zhang, S. Yan, M. Xiao and Z. Zou, *ACS Appl. Mater. Interfaces*, 2014, **6**, 2356.

- 99 Y. P. Xie, G. Liu, L. C. Yin and H. M. Cheng, *J. Mater. Chem.*, 2012, **22**, 6746.
- 100 X. Y. Chen, Y. Zhou, Q. Liu, Z. D. Li, J. G. Liu and Z. G. Zou, *ACS Appl. Mater. Interfaces*, 2012, **4**, 3372.
- 101 X. G. Han, Q. Kuang, M. S. Jin, Z. X. Xie and L. S. Zheng, *J. Am. Chem. Soc.*, 2009, **131**, 3152.
- 102 C. Hu, X. Zhang, W. Li, Y. Yan, G. Xi, H. Yang, J. Li and H. Bai, *J. Mater. Chem. A*, 2014, **2**, 2040.
- 103 M. A. Lukowski, A. S. Daniel, F. Meng, A. Forticaux, L. S. Li and S. Jin, *J. Am. Chem. Soc.*, 2013, **135**, 10274.
- 104 M. Aksit, B. C. Hoselton, H. J. Kim, D.-H. Ha and R. D. Robinson, *ACS Appl. Mater. Interfaces*, 2013, **5**, 8998.
- 105 X. D. Zhang, J. G. Xu, H. Wang, J. J. Zhang, H. B. Yan, B. C. Pan, J. F. Zhou and Y. Xie, *Angew. Chem., Int. Ed.*, 2013, **52**, 4361.
- 106 Y. Q. Shi, S. H. Jiang, K. Q. Zhou, C. L. Bao, B. Yu, X. D. Qian, B. B. Wang, N. N. Hong, P. Y. Wen, Z. Gui, Y. Hu and R. K. K. Yuen, *ACS Appl. Mater. Interfaces*, 2014, **6**, 429.